

論文 / 著書情報
Article / Book Information

Title	Geofluid mapping reveals the connection between magmas, fluids, and earthquakes
Authors	Hikaru Iwamori, Yasuo Ogawa, Tomomi Okada, Tohru Watanabe, Hitomi Nakamura, Tatsu Kuwatani, Kenji Nagata, Atsushi Suzuki, Masahiro Ichiki
Citation	communications earth & environment, Vol. 6
Pub. date	2025, 5
DOI	http://dx.doi.org/10.1038/s43247-025-02351-9
Creative Commons	Information is in the article.

<https://doi.org/10.1038/s43247-025-02351-9>

Geofluid mapping reveals the connection between magmas, fluids, and earthquakes

Check for updates

Hikaru Iwamori¹✉, Yasuo Ogawa², Tomomi Okada³, Tohru Watanabe⁴, Hitomi Nakamura⁵, Tatsu Kuwatani⁶, Kenji Nagata⁷, Atsushi Suzuki⁸ & Masahiro Ichiki³

Subsurface geofluids drive Earth's evolution through seismogenesis, volcanism, and plate motion. Previous geofluid-distribution estimates from various geophysical methods show large variations. To quantify the geofluid distribution, we employ a novel inversion method capable of simultaneously analysing seismic velocity from high-resolution seismic-wave tomography along with electrical conductivity from magnetotelluric data in a volcanic region of Northeast Japan. This study successfully maps the volume and geometrical parameters of aqueous fluids and basaltic and andesitic magmas. A large, slightly leaking fluid reservoir is identified at a depth of 10–20 km. The fluid pressure–depth profile indicates that the seismogenic region corresponds to the area with the highest excess fluid pressure directly above the reservoir. At the bottom of the reservoir near the Moho, the basaltic and andesitic magmatic roots exhibit horizontal distributions to the west and east of the volcanic front, respectively. Andesitic magma is identified directly beneath the front, along with a magma-depleted zone near the Moho. We deduce that magma along the Moho released aqueous fluids, resulting in high pore-fluid pressure that induced earthquakes in the upper crust. Certain magmas ascended to form active volcanoes, leaving behind a magma-depleted zone. Our findings highlight the importance of crustal processes in volcanic-front formation.

Geofluids (e.g. aqueous fluids and magma) in the Earth's interior play an important role in various geodynamic processes; they affect the chemical reactions and physical properties of the crust and mantle. For example, a reduction in rock strength due to the introduction of aqueous fluids can induce seismicity^{1,2}, plate motion³, and subduction⁴. Aqueous fluids expelled from subducting plates can react with the mantle rocks, lowering the rock's melting temperature and producing magma⁵. These aqueous fluids and magmas can rise and result in arc volcanism⁵, seismicity and crustal deformation⁶, and continental crust growth over a long period⁷.

Previous studies employed various observational methods, such as seismic or magnetotelluric (MT) tomography, to elucidate the distribution of geofluids in the Earth's interior. Several parameters, including seismic P- and S-wave velocities (V_P and V_S , respectively), seismic attenuation, and electrical conductivity (σ)^{8–11}, have been used to detect geofluids. Slow seismic velocities with large V_P/V_S ratios and attenuations, or high σ , may be interpreted as an indication of geofluids^{12,13}.

However, determining the presence and distribution of geofluids, particularly in the crust, is difficult. For example, the V_P/V_S ratios of the major rock types that constitute the crust ($V_P/V_S = 1.5–2.0$) exhibit enough diversity to explain the observed variations for scenarios where fluids are absent¹⁴. Furthermore, owing to the relatively high compressibility of aqueous fluids, the V_P/V_S ratio of rocks containing these fluids may decrease (compared to that of dry, intact rocks) depending on the amount of fluid, the geometrical shape of the fluid (as expressed by the aspect ratio), and temperature–pressure conditions¹⁴.

Contrastingly, electrical conductivity is more responsive to the presence of geofluids, and major crustal rocks show relatively low electrical conductivity in the absence of fluids ($<10^{-2}$ S/m)¹⁴ compared to the 1 S/m observed conductivity for arcs and continental crust. Therefore, higher σ values suggest the presence of geofluids. However, determining the exact amount and connectivity of the fluids based solely on the electrical conductivities is difficult^{9,14}.

¹Earthquake Research Institute, The University of Tokyo, Bunkyo, Tokyo, Japan. ²Multidisciplinary Resilience Research Center, Institute of Innovative Research, Tokyo Institute of Technology, Meguro, Tokyo, Japan. ³Research Center for Prediction of Earthquakes and Volcanic Eruptions, Graduate School of Science, Tohoku University, Sendai, Japan. ⁴Department of Earth System Science, Faculty of Sustainable Design, University of Toyama, Toyama, Japan. ⁵Geological Survey of Japan, National Institute of Advanced Industrial Science and Technology (AIST), Tsukuba, Japan. ⁶Institute for Marine Geodynamics, Japan Agency for Marine-Earth Science and Technology (JAMSTEC), Yokosuka, Japan. ⁷Center for Basic Research on Materials (CBRM), National Institute for Materials Science (NIMS), Tsukuba, Ibaraki, Japan. ⁸JX Metals Resources Exploration & Development Co., Ltd, Chiyoda, Tokyo, Japan. ✉e-mail: hiwamori@eri.u-tokyo.ac.jp

As either seismic velocity or electrical conductivity alone is insufficient for constraining the distribution of geofluids, previous studies conducted analyses that combined the two observations^{10,15}. A few studies also conducted quantitative analyses for the combined observations, referred to as ‘joint inversion’ or ‘simultaneous analysis’^{8,14,16,17}. In this study, we applied a recently developed inversion method to simultaneously analyse seismic velocity and electrical conductivity¹⁸ using high-resolution tomographic results^{12,13} to quantitatively map fluid volume and determine the geometrical parameters of the geofluids in the Northeast Japan arc.

Results and discussion

Seismic velocity and electrical conductivity structures

The Northeast Japan arc is geodynamically active, with geological features such as earthquakes, hot springs, volcanoes, and crustal deformation. The study area corresponds to a trench-arc segment that encompasses the hypocentre and ruptured area of ‘the 2011 off the Pacific coast of Tohoku Earthquake’ (Fig. 1). Since 2000, more than 50,000 earthquakes have been recorded in the study area, including the 2008 Iwate-Miyagi Nairiku earthquake [hereinafter referred to as IMN2008, with an M_{JMA} of 7.2 (M_W of 6.9)]. Several Quaternary volcanoes are situated in the area. Of these, Kurikoma Volcano, which consists primarily of andesitic lavas and pyroclastic rocks (ranging from basaltic andesite to dacite), occupies the central part and has experienced frequent eruptions since ~0.5 Ma, with the latest phreatomagmatic eruption occurring in 1944¹⁹. The 2011 Tohoku Earthquake caused the volcanic area to subside by up to 10 cm, creating elliptical depressions, with the horizontal dimensions being 15–20 km²⁰. Notably, more than 90 hot springs have existed in the area since before IMN2008, half of which have temperatures exceeding 80 °C²¹ (Fig. 1). Thus, this area is suitable for studying the relationship between earthquakes, geofluids, and crustal deformation through geofluid mapping.

The seismic structure of the study area was determined based on the tomography results obtained in a previous study¹³, where manually selected P- and S-wave arrival time data from nearly 20,000 earthquakes that occurred during 2006–2012 were used. The grid was set at intervals of 0.0625° (~7 km) in the N-S and E-W directions and depths of 0.0, 2.5, 5.0, 7.5, 10.0, 15.0, 20.0, 25.0, 30.0, 35.0, 40.0, 65.0, 90.0, 120.0, 150.0, and 180.0 km¹³ (Supplementary Fig. 1d). The fitting criterion for the seismic model is the minimisation of the travel time residual by revising the three-dimensional seismic velocity structure. The uncertainty of the velocity was estimated to be up to 3%.

The electrical conductivity structure of the study area was determined based on a three-dimensional (3D) inversion²² of a wide-band MT dataset that covers a range of 0.3–2000 s, consisting of 110 stations spaced 5 km apart. This MT dataset is a compilation of pre-existing^{23,24} and newly obtained datasets (Methods, Supplementary Figs. 1–3, and Supplementary Data). The inversion process utilised the full tensor impedances measured at eight representative periods, logarithmically spanning 0.25–800 s, with a 10% error floor. The model consists of a 1-km horizontal grid mesh in the core zone and an outer coarse mesh that includes the surrounding oceans. The vertical meshes are coarser logarithmically at greater depths. The initial model consists of a uniform Earth with an electrical conductivity of 0.01 S/m and a fixed ocean resistivity of 4 S/m. The final model achieves a root mean square (RMS) value of 1.53 (Methods).

The tomography results at 10 km (Fig. 2a, b) and other depths (Supplementary Figs. 4–7) show that V_P/V_S and $\log_{10} \sigma$ exhibit significant variations mostly from 1.6 to 1.9 and –4 to 1, respectively, with distinct localised features, e.g. a high electrical conductivity region was noted just beneath the IMN2008 hypocentre (Fig. 2b). While V_P and V_S show a high correlation (with a correlation coefficient of 0.956, Fig. 2c), V_P , V_S , V_P/V_S , and $\log_{10} \sigma$ show lower correlation coefficient values (Fig. 2d, e); this trend is particularly noted between seismic velocity and electrical conductivity (0.075, 0.077, and 0.030 for $\log_{10} \sigma$ vs. V_P , V_S , and V_P/V_S , respectively). The low values suggest variable lithology-geofluid combinations with different geofluid parameters (i.e. liquid fraction and geometry); therefore, a simultaneous analysis of seismic velocity and electrical conductivity is necessary¹⁴.

Although V_P and V_S are relatively sensitive to lithological variations and σ is more sensitive to liquid phase variations, they are related through the common parameters, particularly the amount of liquid phase. For instance, in Fig. 2e, data points in red with high σ are estimated to involve geofluids of more than 3 vol%, while some with low σ may also involve the appreciable amounts of geofluids. Discriminating such conditions and quantifying the amount of geofluids require V_P and V_S data, in addition to σ .

In this study, we use a recently developed inversion method to quantitatively estimate the lithology, geofluid type, and relevant fraction and geometrical parameters in relation to the aspect ratio and connectivity of the geofluid phase, based on a simultaneous analysis of V_P , V_S , and σ ^{14,18}. The values for V_P , V_S , and σ come from the final models of seismic tomography and MT inversions separately and then the simultaneous analysis is being done. The optimal solution was obtained probabilistically by applying a marginalisation technique within the Bayesian statistical framework¹⁸ (Methods).

Quantitative mapping of geofluids

The inversion analysis first integrates the probability by grid search over the entire range of the three fluid parameters (ϕ , α , and α_{EC}) for each of the 234 combinations (78 lithologies \times three types of geofluids [aqueous fluid, basaltic magma, and andesitic magma, Methods]). Based on the integrated probability, the most probable lithology-geofluid combination is determined, and then the most probable values of ϕ , α , and α_{EC} are calculated¹⁸. This method does not necessarily minimise the residual between the data and the model for each data point. However, the resulting residuals are mostly within the data uncertainties (Supplementary Figs. 4c, 5c, and 7c), demonstrating the model’s ability to reproduce the observed data effectively. Moreover, the model shows an average probability of 14% (Supplementary Fig. 8), which is well constrained compared to the probability of a uniform distribution (i.e., $1/234 \times 100 = 0.43\%$).

Figure 3a, b shows the most probable distributions of the aqueous fluid and andesitic and parental basaltic magmas in the study area (Supplementary Data). The probabilities (p) of the solutions in the Bayesian framework (Fig. 3c) are relatively high and sharply focused in most areas (>10%), including the deep part around the Moho (Supplementary Fig. 8). In contrast, the p value for the middle crust–shallow part of the western part is relatively low (<10%, Supplementary Fig. 8), and the probability distribution was not sharply focused (e.g., the ‘4%’ case, Fig. 3c). However, stable solutions are obtained to specify the type of geofluid even for the ‘4%’ case (Fig. 3c) and these solutions are well constrained compared to the aforementioned probability of 0.43% for a uniform distribution. In addition, inversion results of a synthetic data set (Supplementary Fig. 9) demonstrate that the three types of geofluids can be reasonably identified and quantified under the crust and uppermost mantle conditions.

The upper rows of Fig. 3a, b show the distribution of aqueous fluid. The most prominent feature is a fluid reservoir with a large amount of aqueous fluid (~10 vol%), distributed at a depth of 10–20 km below the hypocentre of IMN2008 (Fig. 4). We observe an inverse correlation between earthquake frequency and the aqueous fluid volume. The maximum number of earthquakes occurred at a depth of 5–6 km; the number of earthquakes decreases with depth, whereas the amount of fluid increases (Fig. 4). Notably, earthquakes rarely occurred in the fluid reservoir.

In this reservoir located under the hypocentre of IMN2008, the fluid volume, ϕ , decreases from ~10% (at a depth of 20 km) to 0.1% (at a depth of ~30 km, Fig. 4a). For the depth of 20–30 km, the average value of α_{EC} (a threshold fluid fraction to achieve liquid-phase connection and efficient electrical conduction) is 0.1–0.01%, lower than the fraction of aqueous fluid; this suggests that the fluid is connected throughout the depth range (Supplementary Fig. 10). Magma exists just below this depth, and the fluid is rooted in the magma (Fig. 4a) that spreads along the Moho (Fig. 5 and Supplementary Fig. 11 for depth slices).

Notably, the magma does not spread homogeneously along the Moho and exhibited distinct spatial and compositional variations. Basaltic magma is distributed mostly in the uppermost mantle and on the western side of the

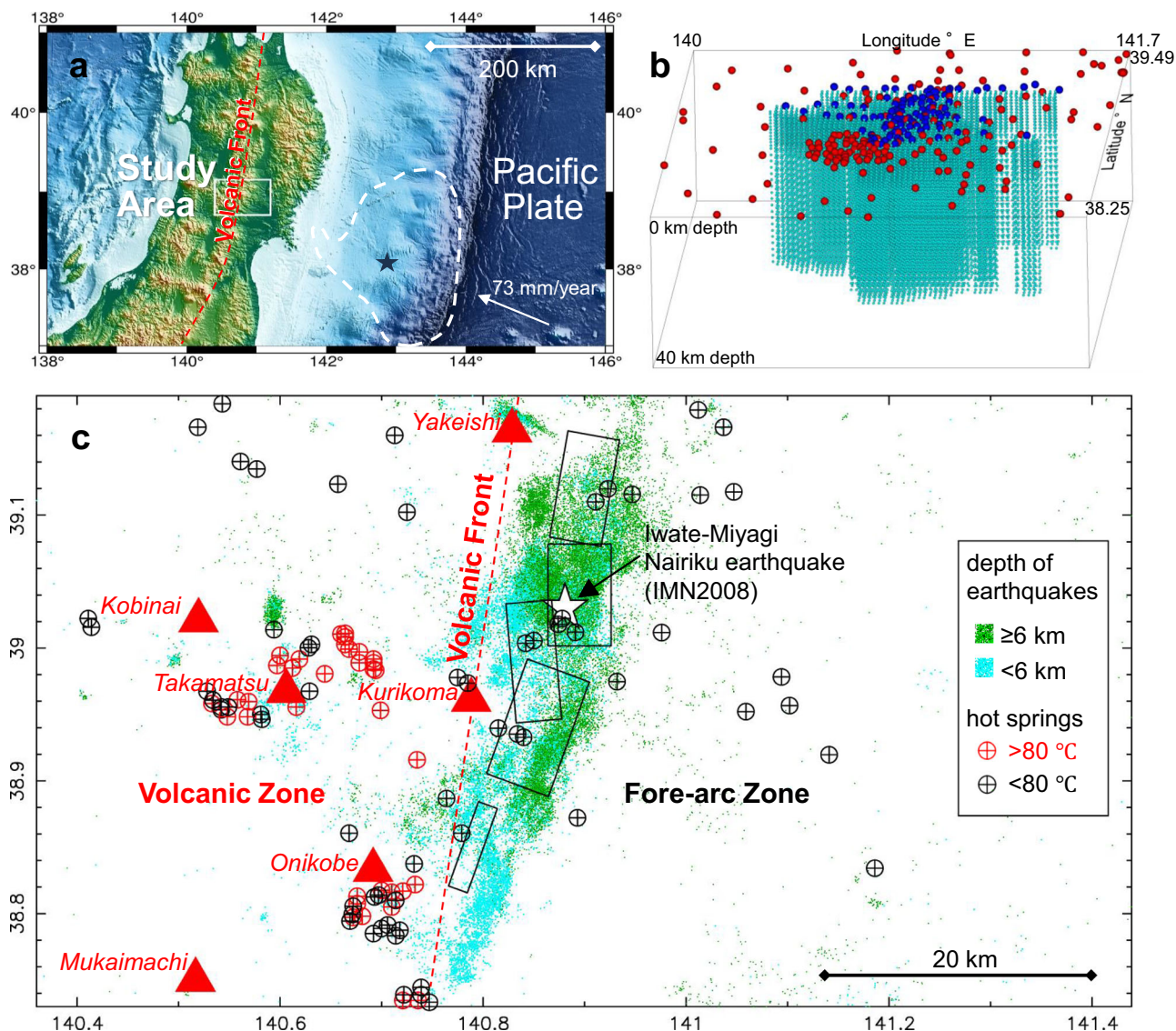


Fig. 1 | Index maps of the study area. **a** Study area in the Northeast Japan arc subducted by the Pacific plate, with the relative velocity being 73 mm/yr³⁸. The figure illustrates the hypocentre and ruptured area of ‘the 2011 off the Pacific coast of Tohoku Earthquake’ (solid star and white broken line, respectively)³⁹ and the volcanic front (red dashed line). **b** The seismic and magnetotelluric (MT) stations (181 red circles and 110 blue circles, respectively) considered for this study and the inversion grid nodes of 20367 points (small sky-blue circles) for which the P- and

S-wave seismic velocities and electrical conductivity were obtained (Supplementary Fig. 1). **c** Epicentres of 51,358 earthquakes that occurred during 2000–2018 (small green dots have depths ≥ 6 km and light-blue dots have depths <6 km); the open star indicates the hypocentre of the 2008 Iwate-Miyagi Nairiku earthquake (IMN2008) of the magnitude $M_j = 7.2$ ⁴⁰. The five boxes represent the fault planes associated with IMN2008⁴¹. Quaternary volcanoes are shown using red triangles⁴², and hot springs⁷¹ are shown using circles.

study area (under the volcanic zone, Figs. 1 and 3b). It is barely detected in the shallow crust and was not observed directly under the volcano. Contrastingly, andesitic magma is identified in the shallow part, including the areas directly beneath the volcanoes, as well as being widely distributed near the Moho (under the fore-arc zone, Figs. 1 and 3b). We observe a magma-depleted region (gap) near the Moho (Fig. 5) between the basaltic magma distributed mainly on the western side and the andesitic magma distributed in the east, suggesting that the magma that originally spread near the Moho ascended above this gap to feed the volcanoes (Fig. 5).

Magma, fluid, and earthquake connection

In Northeast Japan, the addition of fluid from the subducted Pacific Plate to the mantle wedge initiates mantle melting at depths between 70 and 90 km⁵, which produces basaltic magma that ascends towards the Moho. This magma loses buoyancy, owing to the changes in lithology and rock density at the Moho (Supplementary Fig. 12), spreading laterally²⁵ to the fore- and back-arc zones. Although the back-arc zone is outside our study area, a low-

velocity anomaly in this zone has been reported previously¹³, which could be attributed to a westward migration of magma. During this lateral migration, basaltic magma cools and undergoes crystallisation, producing the andesitic magma in the fore-arc zone (Fig. 5). Solidification occurs in the marginal part of the magma-rich region near the Moho, and the aqueous fluid components dissolved in the magma are gradually expelled, forming a fluid reservoir under the IMN2008 hypocentre (Fig. 5).

During the gradual fluid expulsion that occurs at a depth of 32 km (Point A, Fig. 4b), the pressures of the aqueous fluid, magma, and host rock are nearly equal in the quasi-equilibrium state. However, at the surface (Point B), the fluid pressure is close to atmospheric or slightly higher, as indicated by the artesian springs. The fluid between points A and B is interconnected, as previously described, and the fluid pressure decreases with the vertical distance from Point A, influenced by fluid velocity and permeability, until reaching the atmospheric pressure at Point B. The numerical solution satisfying these conditions (see Methods) revealed large excess pressure from the central–shallow regions of the crust. Particularly,

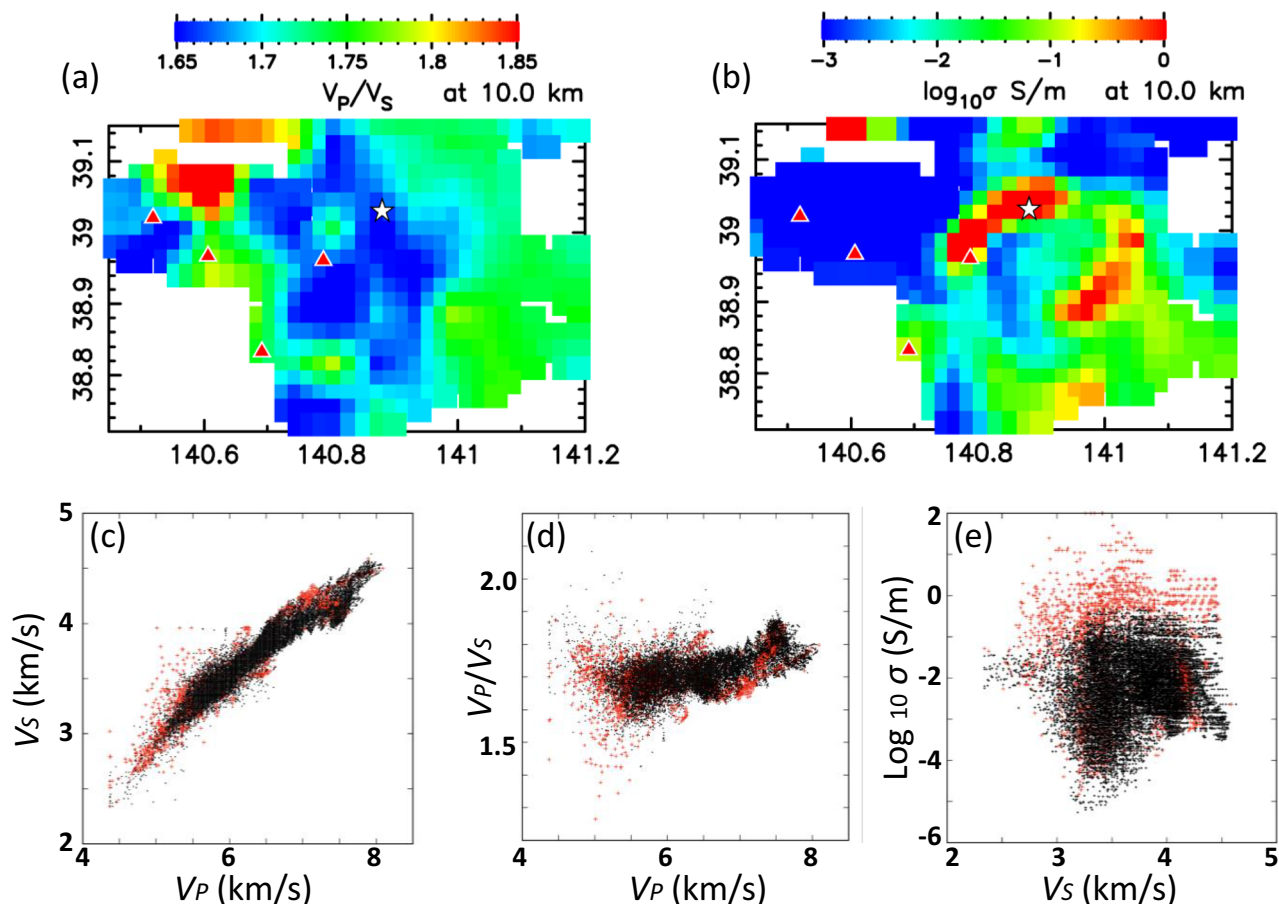


Fig. 2 | Seismic velocity and electrical conductivity in the study area. Horizontal distribution of (a) V_p/V_s and (b) electrical conductivity ($\log_{10} \sigma$) at 10-km depth. The white star denotes the epicentre of the 2008 Iwate-Miyagi Nairiku earthquake (IMN2008), and the small red triangles represent the Quaternary volcanoes, with the

easternmost corresponding to the Kurikoma Volcano on the volcanic front (Fig. 1). Correlations between (c) V_p and V_s , (d) V_p and V_p/V_s , and (e) V_s and $\log_{10} \sigma$. Data points with estimated geofluid volumes greater than 3% (Supplementary Data) are shown in red.

the depth range where the fluid pressure exceeds the lithostatic pressure by >200 MPa corresponds to the seismic activity zone (Fig. 4b), implying that the aqueous fluid induced earthquakes in the region (including the IMN2008). At the depth of the fluid reservoir, in addition to the lower excess pressure of the fluid, the higher temperature promotes plastic deformation, thereby suppressing seismicity.

In addition to the high seismicity area surrounding the IMN2008 hypocentre, we observe another high seismicity area in the shallower crust (<6 km in depth) south of Kurikoma Volcano (Fig. 1); no significant fluid reservoir existed in the subsurface of this region. Earthquakes in the southern area occurred along multiple fault planes (roughly running N-S, with E-W compressional displacement) associated with IMN2008 and its fault plane (Fig. 1).

Notably, in the eastern part of the study area (on the trench side of the volcanic front, Fig. 1), including the IMN2008 region and the above-mentioned high seismicity areas, the magma is present near the Moho (Figs. 3b, 5, and Supplementary Fig. 11). The presence of magma deep in the fore-arc zone suggests that the location of the volcanic front was not solely determined by the magma distribution in the mantle wedge. The mantle processes that occur at depths of 50–200 km, including the dehydration of a subducted plate, distribution of temperature and melting within the mantle wedge, and melt migration dynamics, may control and define the positions of volcanic fronts^{26,27}. However, our results suggest that the magma supplied from the mantle may spread near the Moho, with the location of the volcanic front remaining unknown. Although the mantle processes described in this section contribute to the formation of the volcanic front, our results suggest that the processes that occur around the Moho and at shallower depths, e.g.

horizontal migration and crystallisation along the Moho and the subsequent ascent of magma (Fig. 5) and structural control associated with reactivation of the numerous Miocene faults in the volcanic zone under across-arc compression since ~ 3.5 Ma²⁸, play an important role in the formation of volcanic fronts in the Northeast Japan arc.

Geofluid mapping of our study requires a high-resolution dataset including seismic velocities and electrical conductivity. Such datasets have been relatively rare; however, once the dataset is constructed, our study can provide a reliable framework for determining the volume, geometrical parameters, and pressure of aqueous fluid phase and different magma types in complex tectonic settings, thereby fuelling detailed studies on geofluid dynamics, crustal deformation, and earthquakes, in the fields of geodynamics, geoengineering, and disaster mitigation sciences.

Methods

Magnetotelluric (MT) inversion

The MT method²⁹ is an electromagnetic geophysical method that measures the electrical resistivity of the Earth's sub-surface. The method uses natural electromagnetic signals that originate from volcanic lightning (period <1 s) and magnetospheric storms (period >1 s). We measured the electromagnetic fields in a wide period band (between 3 ms and 2000 s) and estimated the impedance tensors as the Earth's response functions for each period and location. Then, we carried out 3D inversion modelling²² to obtain a 3D conductivity structure that could explain the observed impedance tensor with minimum model features. In this study, the inversion started with a uniform earth model ($\sigma = 0.01$ S/m), while

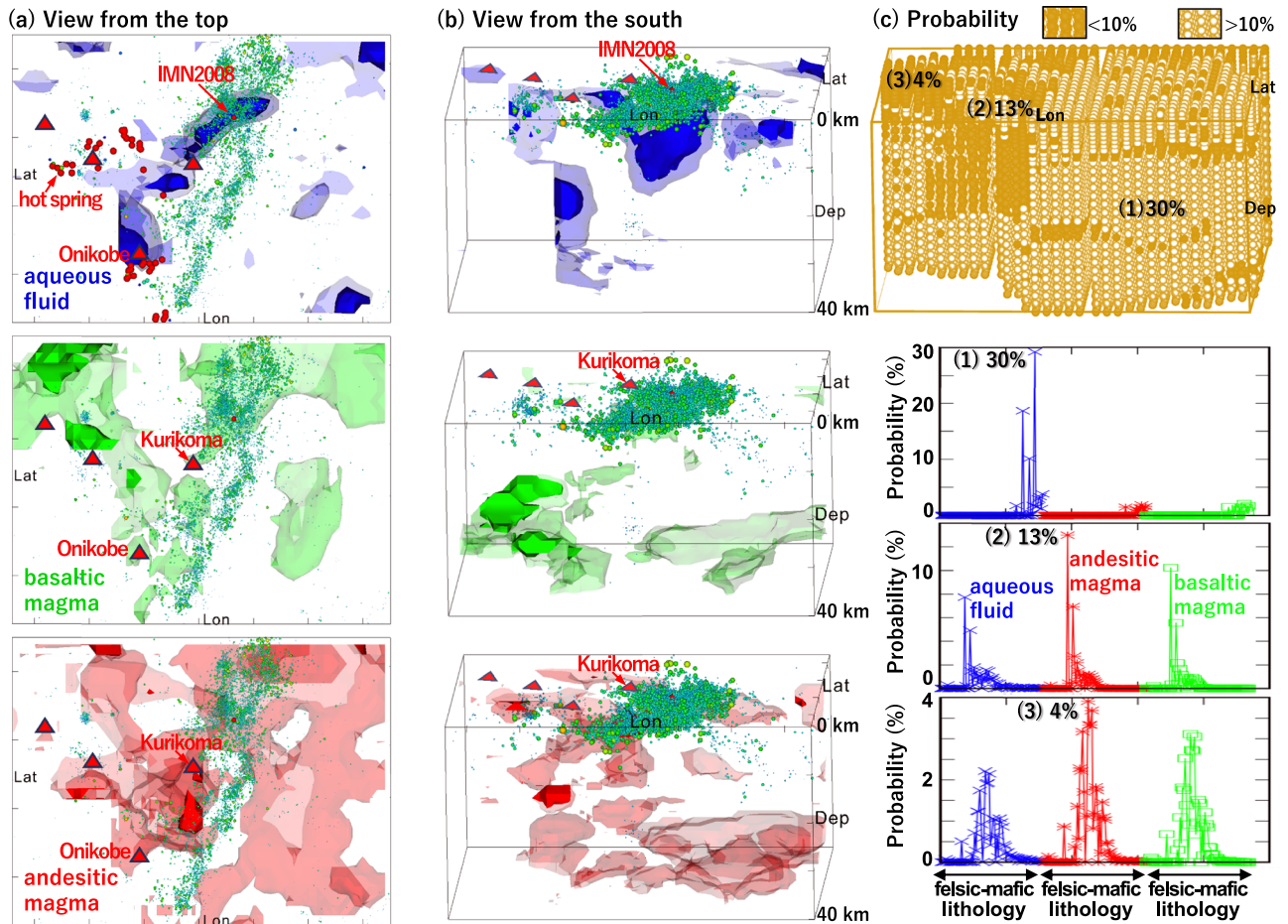


Fig. 3 | Geofluid map and the probability. Distribution of aqueous fluid and basaltic and andesitic magmas for 140.45–141.15°E, 38.72–39.15°N, at depths ranging from 1–40 km. Views from the (a) top and (b) south for saline aqueous fluid (blue, upper row) and basaltic (green, mid row) and andesitic (red, bottom row) magmas. In a, b the dark-coloured regions (with 10 vol% geofluids) are surrounded by pale transparent regions (3 vol%). The probabilities for the optimal solutions in a, b are

shown in (c), presenting three examples (at three grid nodes) of the probability distribution, including the 234 lithology-geofluid combinations (78 lithologies × three types of geofluids). The 78 lithologies range from felsic to ultramafic in composition (horizontal axis of the three example diagrams). The three types of geofluids represent the aqueous fluid (blue) and andesitic (red), and basaltic (green) magmas.

Fig. 4 | Vertical profiles of the geofluid parameters. a The average volume profile of liquid phases beneath the IMN2008 hypocentre (Fig. 3). The range in volume at each depth is shown as an error bar. The frequency of earthquakes shown in Fig. 1 is the highest (~10,000) in the area directly above the fluid reservoir with $\log_{10} \phi \sim -1$. In b line (2) represents the calculated pressure profile of the flowing aqueous fluid (see Methods), with reference to the hydrostatic profiles shown by lines (1) and (3). The excess fluid pressure, ΔP , over the lithostatic pressure is denoted by the red line.

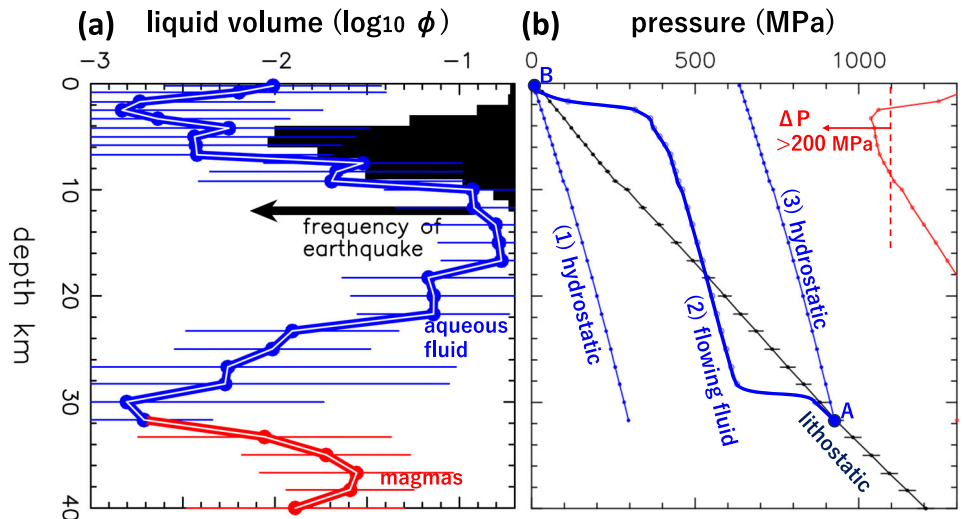
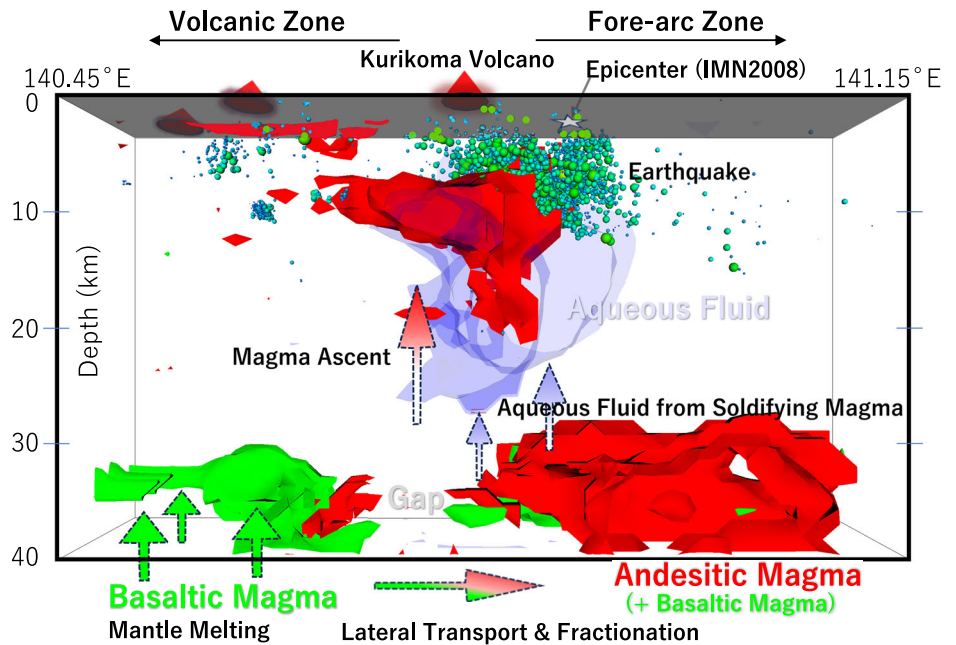


Fig. 5 | Geofluid map showing the connection between magmas, aqueous fluids, earthquakes, and volcanoes. Distribution of geofluids (with >3 vol%) and the across-arc E-W structure between 140.45°–141.15°E and 38.95°–39.05°N, showing the relationships between basaltic (green) and andesitic (red) magmas, aqueous fluid (pale blue), earthquakes, and volcanoes.



assuming a fixed distribution of the surrounding ocean. The procedure was iterated owing to the nonlinearity of the problem. We used the MT inversion code of ref. 22. We inverted full components of impedance tensor with 10% error floor. The initial model and the prior model are a 100 Ω m uniform earth with 0.25 Ω m ocean. The RMS of the initial model is 10.09. The inversions were iterated with changing the trade-off parameter ‘lambda’, and the smallest RMS model was found as the best model. Then, the best model was used as the initial and prior model to obtain the second-generation best model. This procedure was repeated for five-times and the RMS of 1.53 was reached.

Constraints and prior information considered in this study

The volcanoes in the study area, represented by Kurikoma Volcano, are located approximately along the volcanic front of the Northeast Japan Arc (Fig. 1). The volcanic rocks contain phenocrysts consisting of plagioclase, clinopyroxene, orthopyroxene, opaque minerals, and olivine¹⁹. Some major element concentrations (but not complete sets), such as SiO₂ and FeO/MgO in bulk rock compositions, have been reported in the literature¹⁹; the lavas from Kurikoma Volcano are mostly andesitic and exhibit a continuous trend from basaltic andesite to dacite (with the SiO₂ content ranging from 56 wt% to 66 wt%), suggesting a fractionation trend from basaltic magma. Based on these observations, we use the reported compositions of IW17 and HM01^{30,31}, which are representative of the relatively undifferentiated basaltic and andesitic magmas along the volcanic front of the Northeast Japan Arc, with the SiO₂ contents being 51.4 and 60.9 wt% and FeO/MgO being 1.3 and 1.6, respectively; both IW17 and HM01 are estimated to contain 5 wt% H₂O^{30,31}.

The saline aqueous fluids in the study area represent the deep-seated fluids derived from either the magmas³² and/or the subducting plate beneath the Japan arcs³³. Based on the composition of the spring water with the highest salinity observed in the study area, we estimate that the NaCl concentration in the aqueous fluid is 2 wt%. We use the above-mentioned compositions for the inversion calculation (for the basaltic and andesitic magmas and aqueous fluid), to map the geofluids with probability.

The geothermal gradient and depth–temperature relation used in this study are based on the crustal heat flow observations presented in the literature³⁴ and the numerical simulations accounting for mantle convection

using the structure shown in a previous work¹⁴. Compared with that in the fore-arc zone, the heat flow in the volcanic zone to the west of the volcanic front is discontinuously higher³⁴, where active volcanoes occur, and hot magmas ascend to the surface (Fig. 1). Based on these observations, we assume that the temperatures are 1100 and 900 °C for the basaltic and andesitic magmas, respectively, to calculate the physical properties of the magmas in the volcanic zone.

We consider 78 rock types¹⁴, which cover the observed seismic velocities sufficiently, with relatively no bias, to obtain the most probable solutions for lithology, geofluid type (aqueous fluid, basaltic magma, andesitic magma), ϕ (geofluid volume), α (aspect ratio of pore filled by geofluids)³⁵, and α_{EC} (threshold fraction required to achieve liquid-phase connection)¹⁴.

Probabilistic inversion method

To obtain the most probable solution, in addition to the values of V_P , V_S , and σ , we utilise the near-surface observations (heat flow and the compositions of lavas and spring waters that were described in the previous section) as prior knowledge. We calculate the probabilities of the presence of these geofluids, including saline aqueous fluid, andesitic magma that appears on the surface, and basaltic magma that is potentially seated at different depths as a parent magma, determining combinations with 78 lithologies and variable geometrical parameters of the geofluid phase as below.

In this study, we use a new probabilistic inversion method in the Bayesian statistical framework¹⁸ to estimate the following parameters. [1] The 78 possible lithologies are labelled using discrete variables i_A ($=1, 2, \dots, 78$); these encompassed felsic–ultramafic rocks (including sedimentary, metamorphic, and igneous rocks¹⁴). [2] The geofluid types (aqueous fluid or basaltic magma or andesitic magma) are labelled as discrete variables i_B ($=1, 2, 3$). [3] The geofluid amount (volume fraction, ϕ , ranging from 10^{-7} to 1) is determined as a continuous variable. [4] We determine the parameters related to fluid geometry (aspect ratio, α , from 10^{-5} to 1) and the critical fluid fraction related to connectivity (α_{EC} , from 10^{-5} to 1) as continuous variables,¹⁴ based on the V_P , V_S , and σ data obtained from the tomography results.

The detailed calculation procedure used in this study is outlined in a previous study¹⁸. The method uses a marginalisation technique that first estimates the values of i_A and i_B and then quantifies the values of ϕ , α , and

α_{EC} . This method is robust and can be reliably used for lithology and geofluid-type determination, as indicated by the inversion tests conducted in a previous study using synthetic datasets¹⁸. By using the forward model¹⁴, we calculate the P-wave velocity (f_p), S-wave velocity (f_s) and electrical conductivity (f_σ) for a given set of i_A , i_β , ϕ , α , α_{EC} , geofluid composition (major-element compositions of the magmas and salinities of aqueous fluids), pressure, and temperature at each grid node (Fig. 1b). The geofluid compositions are constrained based on the observations of the lavas and hot-spring waters, and the pressure and temperature are constrained by the surface heat flow and numerical simulations for a coupled system of plate subduction, induced mantle convection in the wedge, and heat conduction in the overriding crust¹⁴. For each grid node, all combinations of i_A , i_β , ϕ , α , and α_{EC} were examined based on the evaluation function, E_0 [see Eq. (1)] as the negative logarithm of the joint posterior probability, p , of the unknown parameters (i_A , i_β , ϕ , α , and α_{EC}), based on the tomography results.

$$E_0(i_A, i_\beta, \phi, \alpha, \alpha_{EC}) \equiv -\ln p(i_A, i_\beta, \phi, \alpha, \alpha_{EC} | V_P, V_S, \sigma) \\ = \{V_P - f_p(i_A, i_\beta, \phi, \alpha, \alpha_{EC})\}^2 / (2s_P^2) \\ + \{V_S - f_s(i_A, i_\beta, \phi, \alpha, \alpha_{EC})\}^2 / (2s_S^2) \\ + \{\log_{10}\sigma - \log_{10}f_\sigma(i_A, i_\beta, \phi, \alpha, \alpha_{EC})\}^2 / (2s_\sigma^2) + C \quad (1)$$

where s_P , s_S , and s_σ represent the standard deviations of the uncertainties in V_P , V_S , and $\log_{10}\sigma$, respectively, and C is a constant that is independent of the unknown parameters. In this study, $2s_P$ and $2s_S$ represent 3.0% of the observed V_P and V_S , according to Okada et al.¹³, and the value of $2s_\sigma$ is 0.5 for the $\log_{10}\sigma$, according to Ogawa et al.¹².

First, the most probable combination of i_A and i_β was selected to minimise $\Sigma_{\phi, \alpha, \alpha_{EC}}\{E_0(i_A, i_\beta, \phi, \alpha, \alpha_{EC})\}$, which corresponded to the maximisation of the marginalised posterior probability of i_A and i_β , based on the tomography results, $p(i_A, i_\beta | \phi, \alpha, \alpha_{EC}, V_P, V_S, \sigma)$. Note that the summation symbol $\Sigma_{x,y}\{F(x, y, z)\}$ indicates the summation of $F(x, y, z)$ over all possible combinations of x and y .

Then, using the selected i_A^\dagger and i_β^\dagger values, the most probable values of ϕ , α , and α_{EC} were calculated by minimising $E_0(i_A^\dagger, i_\beta^\dagger, \phi, \alpha, \alpha_{EC})$, which corresponded to the maximisation of the posterior probability of ϕ , α , and α_{EC} , given i_A^\dagger , i_β^\dagger , V_P , V_S , and σ , $p(\phi, \alpha, \alpha_{EC} | i_A^\dagger, i_\beta^\dagger, V_P, V_S, \sigma)$. The probability of lithology-geofluid combinations in the main text corresponds to the abovementioned marginalised posterior probability, $p(i_A, i_\beta | \phi, \alpha, \alpha_{EC}, V_P, V_S, \sigma)$, calculated using the following equation:

$$\Sigma_{\phi, \alpha, \alpha_{EC}} \left[\exp \left\{ -E_0(i_A, i_\beta, \phi, \alpha, \alpha_{EC}) \right\} \right] / \\ \Sigma_{i_A, i_\beta, \phi, \alpha, \alpha_{EC}} \left[\exp \left\{ -E_0(i_A, i_\beta, \phi, \alpha, \alpha_{EC}) \right\} \right]. \quad (2)$$

In this inversion analysis of V_P , V_S , and σ , spatial smoothing was not applied to avoid duplicated smoothing, in addition to the spatial smoothing already applied in the individual seismic and MT inversions. Nonetheless, it is likely that some important structures, such as low-velocity anomalies, tend to be under-recovered, leading to an underestimation of geofluid fraction ϕ . In this respect, the estimated ϕ of the geofluid-abundant regions in Figs. 3–5 is likely to represent a minimum value, providing strong evidence for the presence of geofluids.

Fluid flow and pressure

In the area around the hypocentre of IMN2008, ϕ exceeds 0.1% for the entire depth range (from the top near the surface to the root of the aqueous fluids at 32 km depth); this includes the fluid reservoir ($\phi \sim 10\%$) at a depth of ~ 10 – 20 km (Supplementary Fig. 10). For this depth range, the average value of α_{EC} is less than 0.1% (Supplementary Fig. 10), suggesting that the fluid is connected throughout the depth profile. When the connected fluid is stationary, the fluid pressure gradient follows the hydrostatic pressure gradient, and the two cases (starting from the surface and the root of the aqueous

fluid) provided the lower and upper bounds of the hydrostatic pressure [lines (1) and (3) in Fig. 4b, respectively]. When the connected fluid flows, the pressure gradient, ∇P , deviates from the hydrostatic pressure gradient in accordance with the flow velocity (V_{af}) and permeability (k_ϕ), which can be expressed as follows³⁶:

$$V_{af} = -k_\phi \nabla P / \eta_\phi, \text{ and } k_\phi = R^2 \phi^3 / B \quad (3)$$

where the viscosity of the aqueous fluid, η_ϕ , is set at 10^{-3} Pa s³⁷, the mineral grain size of the permeable rock is set as 10^{-3} m, and the constant B is set as 10^3 ³⁶. This equation involves the viscous force between the fluid flow and the rocks, which decreases the fluid pressure along the flow. By using the average ϕ at each depth shown in Fig. 4a and assuming a constant fluid flux, ϕV_{af} , over the entire depth range, we numerically solved the equation for the depth variation of P , to satisfy both the atmospheric pressure at the surface (Point B, Fig. 4b) and the lithostatic pressure at the depth of 32 km (Point A; as illustrated by line (2) in Fig. 4b). The calculated ϕV_{af} value is 2.1×10^{-10} m/s per unit area, comparable to the average discharge rate of groundwater in the study area²¹ ($\sim 10^{-10}$ m/s, based on the discharge rate of 10^{-2} km³/year over an area of ~ 3000 km²). If the fluid flux is not constant, e.g. the aqueous fluid reservoir with $\phi \sim 10\%$ supplied the fluid to the shallow depth (without any influx from the deeper part), the depth profile of P has more similarities with line (3), indicating more excess pressure at shallow depths (< 10 km). In any case, emptying the aqueous fluid reservoir (with the estimated fluid volume being ~ 3000 km³) would require ~ 0.3 million years, based on the outflux estimated in this study. Therefore, the fluid reservoir is not rapidly tapped but leaks weakly.

Data availability

Source data of the seismic velocity and electrical conductivity structures and the inversion results are available at <https://doi.org/10.6084/m9.figshare.28916048>.

Code availability

The executable code to calculate seismic velocities and electrical conductivity for a given set of lithology-geofluid assemblage and parameters (termed ‘forward model’) is provided in Iwamori et al.¹⁴, and based on the forward model, the inversion procedure to estimate lithology-geofluid parameters for a given set of seismic velocities and electrical conductivity are provided in Kuwatani et al.¹⁸.

Received: 2 October 2024; Accepted: 2 May 2025;

Published online: 22 May 2025

References

- Sibson, R. H. Rupturing in overpressured crust during compressional inversion—the case from NE Honshu, Japan. *Tectonophysics* **473**, 404–416 (2009).
- Hasegawa, A. et al. Change in stress field after the 2011 great Tohoku-Oki earthquake. *Earth Planet. Sci. Lett.* **355–356**, 231–243. <https://doi.org/10.1016/j.epsl.2012.08.042> (2012).
- Kawakatsu, H. et al. Seismic evidence for sharp lithosphere-asthenosphere boundaries of oceanic plates. *Science* **324**, 499–502 (2009).
- Seno, T. & Kirby, S. H. Formation of plate boundaries: the role of mantle volatilization. *Earth Sci. Rev.* **129**, 85–99 (2014).
- Iwamori, H. Transportation of H₂O beneath the Japan arcs and its implications for global water circulation. *Chem. Geol.* **239**, 182–198 (2007).
- Nishimura, T., Hiramatsu, Y. & Ohta, Y. Episodic transient deformation revealed by the analysis of multiple GNSS networks in the Noto Peninsula, central Japan. *Sci. Rep.* **13**, 8381 (2023).
- Campbell, I. H. & Taylor, S. R. No water, no granites - No oceans, no continents. *Geophys. Res. Lett.* **10**, 1061–1064 (1983).

8. Eberhart-Phillips, D., Stanley, W. D., Rodriguez, B. D. & Lutter, W. J. Surface seismic and electrical methods to detect fluids related to faulting. *J. Geophys. Res. Solid Earth* **100**, 12919–12936 (1995).
9. Carcione, J. M., Ursin, B. & Nordskag, J. I. Cross-property relations between electrical conductivity and the seismic velocity of rocks. *Geophysics* **72**, 193–204 (2007).
10. Hammer, P. T. C., Clowes, R. M., Cook, F. A., Vasudevan, K. & van der Velden, A. J. The big picture: a lithospheric cross section of the North American continent. *Geol. Soc. Am. Today* **21**, 4–10 (2011).
11. Evans, R. L., Wannamaker, P. E., McGary, R. S. & Elsenbeck, J. Electrical structure of the central Cascadia subduction zone: the EMSLAB Lincoln Line revisited. *Earth Planet. Sci. Lett.* **402**, 265–274 (2014).
12. Ogawa, Y., Ichiki, M., Kanda, W., Mishina, M. & Asamori, K. Three-dimensional magnetotelluric imaging of crustal fluids and seismicity around Naruko volcano, NE Japan. *Earth Planets Space* **66**, 158 (2014).
13. Okada, T. et al. Seismic velocity structure in and around the Naruko volcano, NE Japan, and its implications for volcanic and seismic activities. *Earth Planets Space* **66**, 114 (2014).
14. Iwamori, H. et al. Simultaneous analysis of seismic velocity and electrical conductivity in the crust and the uppermost mantle: a forward model and inversion test based on grid search. *J. Geophys. Res. Solid Earth* **126**, e2021JB022307 (2021).
15. The MELT Seismic Team. Imaging the deep seismic structure beneath a mid-ocean ridge: the MELT Experiment. *Science* **280**, 1215–1218 (1998).
16. Moorkamp, M. Integrating electromagnetic data with other geophysical observations for enhanced imaging of the Earth: a tutorial and review. *Sur. Geophys.* **38**, 935–962 (2017).
17. Wang, Y., Jia, Z. & Lu, W. SEMI net: seismic-electromagnetic joint inversion network. *IEEE Trans. Geosci. Remote Sens.* **62**, 1–15 (2024).
18. Kuwatani, T., Nagata, K., Sakai, T. & Iwamori, H. Bayesian inversion of lithology and liquid phase parameters from seismic velocity and electrical conductivity in the crust and uppermost mantle. *J. Geophys. Res. Solid Earth* **128**, e2023JB026836 (2023).
19. Fujinawa, A., Fujita, K., Takahashi, M., Umeda, K. & Hayashi, S. Development history of Kurikoma Volcano, Northeast Japan. *Bull. Volcanol. Soc. Jpn.* **46**, 269–284 (2001).
20. Takada, Y. & Fukushima, Y. Volcanic subsidence triggered by the 2011 Tohoku earthquake in Japan. *Nat. Geosci.* **6**, 637–641 (2013).
21. Asamori, K., Umeda, K., Ishimaru, T. & Komatsu, R. Information of geological features of the Japanese Islands. Japan Nuclear Cycle Development Institute, JNC TN7450 2002-003. In Japanese. <https://irdb.nii.ac.jp/01329/0002448747> (2003).
22. Siripunvaraporn, W. & Egbert, G. WSINV3DMT: vertical magnetic field transfer function inversion and parallel implementation. *Phys. Earth Planet.* **173**, 317–329 (2009).
23. Mishina, M. Distribution of crustal fluids in Northeast Japan as inferred from resistivity surveys. *Gond. Res.* **16**, 563–571 (2009).
24. Ichihara, H. et al. A 3-D electrical resistivity model beneath the focal zone of the 2008 Iwate-Miyagi Nairiku earthquake (M 7.2). *Earth Planets Space* **66**, 50 (2014).
25. Lister, J. R. & Kerr, R. C. Fluid-mechanical models of crack propagation and their application to magma transport in dykes. *J. Geophys. Res. Atmos.* **96**, 10049–10077 (1991).
26. Tatsumi, Y. Formation of the volcanic front in subduction zones. *Geophys. Res. Lett.* **13**, 717–720 (1986).
27. Spiegelman, M. & McKenzie, D. Simple 2-D models for melt extraction at mid-ocean ridges and island arcs. *Earth Planet. Sci. Lett.* **83**, 137–152 (1987).
28. Sato, H. The relationship between late Cenozoic tectonic events and stress field and basin development in northeast Japan. *J. Geophys. Res.* **99**, 22261–22274 (1994).
29. Chave, A. D. & Jones, A. G. *The Magnetotelluric Method: Theory and Practice* (Cambridge University Press, 2012).
30. Kuritani, T., Yoshida, T., Kimura, J. I., Hirahara, Y. & Takahashi, T. Water content of primitive low-K tholeiitic basalt magma from Iwate Volcano, NE Japan arc: implications for differentiation mechanism of frontal-arc basalt magmas. *Mineral. Petrol.* **108**, 1–11 (2014).
31. Ueki, K. & Iwamori, H. Density and seismic velocity of hydrous melts under crustal and upper mantle conditions. *Geochem. Geophys. Geosyst.* **17**, 1799–1814 (2016).
32. Shinohara, H., Iiyama, T. & Matsuo, S. Partition of chlorine compounds between silicate melt and hydrothermal solutions: I. Partition of NaCl-KCl. *Geochim. Cosmochim. Acta* **53**, 2617–2630 (1989).
33. Kusuda, C., Iwamori, H., Nakamura, H., Kazahaya, K. & Morikawa, N. Arima hot spring waters as a deep-seated brine from subducting slab. *Earth Planets Space* **66**, 119 (2014).
34. Tanaka, A., Yamano, M., Yano, Y. & Sasada, M. Geothermal gradient and heat flow data in and around Japan (I): appraisal of heat flow from geothermal gradient data. *Earth Planets Space* **56**, 1191–1194 (2014).
35. Takei, Y. Effect of pore geometry on V_p/V_s : from equilibrium geometry to crack. *J. Geophys. Res. Solid Earth* **107**, ECV 6-1–ECV 6-12 (2002).
36. McKenzie, D. The generation and compaction of partially molten rock. *J. Petrol.* **25**, 713–765 (1984).
37. Iwamori, H. Transportation of H₂O and melting in subduction zones. *Earth Planet. Sci. Lett.* **160**, 65–80 (1998).
38. Sella, G. F., Dixon, T. H. & Mao, A. REVEL: a model for Recent plate velocities from space geodesy. *J. Geophys. Res. Solid Earth* **107**, ETG 11-1–ETG 11-30 (2002).
39. Geospatial Information Authority of Japan. Crustal movements in the Tohoku District (in Japanese). *Rep. Coord. Comm. Earthq. Pred. Jpn.* **86**, 184–272 (2011).
40. Japan Meteorological Agency. *Hypocenters. The Seismological Bulletin of Japan*. (Japan Meteorological Agency, accessed 27 January 2024); https://www.data.jma.go.jp/svd/eqev/data/bulletin/hypo_e.html.
41. Takada, Y., Kobayashi, T., Furuya, M. & Murakami, M. Coseismic displacement due to the 2008 Iwate-Miyagi Nairiku earthquake detected by ALOS/PALSAR: preliminary results. *Earth Planets Space* **61**, e9–e12 (2009).
42. Geological Survey of Japan. *Quaternary Volcanoes of Japan*. (Geological Survey of Japan, accessed 27 January 2024); https://gbank.gsj.jp/volcano/Quat_Vol/index_e.html.

Acknowledgements

We would like to thank the members of the Geofluid Mapping Team for their valuable discussions. This work was supported by KAKENHI (grant numbers JP21109006, JP21109003, and JP26109006), awarded to H.I., Y.O., T.O., T.W., and H.N., as well as by the 2nd and 3rd Earthquake and Volcano Hazards Observation and Research Programs (MEXT, Japan), awarded to H.I., T.W., and H.N. Additionally, T.K. and K.N. received funding from the Japan Science and Technology Agency (JST) CREST (grant number JPMJCR1761).

Author contributions

H.I. designed the study; Y.O., A.S., M.I., and T.O. conducted the geophysical tomography; H.I., T.W., and H.N. analysed the petrological/geochemical data; H.I., T.K., and K.N. performed the inversion analysis; and all authors discussed the results to jointly write the manuscript.

Competing interests

The authors declare no competing interests.

Additional information

Supplementary information The online version contains supplementary material available at <https://doi.org/10.1038/s43247-025-02351-9>.

Correspondence and requests for materials should be addressed to Hikaru Iwamori.

Peer review information *Communications Earth & Environment* thanks Martyn Unsworth, Jared Peacock, and Michele Paulatto, reviewer(s) for their contribution to the peer review of this work. Primary Handling Editors: Jan Dettmer and Joe Aslin. [A peer review file is available].

Reprints and permissions information is available at <http://www.nature.com/reprints>

Publisher's note Springer Nature remains neutral with regard to jurisdictional claims in published maps and institutional affiliations.

Open Access This article is licensed under a Creative Commons Attribution-NonCommercial-NoDerivatives 4.0 International License, which permits any non-commercial use, sharing, distribution and reproduction in any medium or format, as long as you give appropriate credit to the original author(s) and the source, provide a link to the Creative Commons licence, and indicate if you modified the licensed material. You do not have permission under this licence to share adapted material derived from this article or parts of it. The images or other third party material in this article are included in the article's Creative Commons licence, unless indicated otherwise in a credit line to the material. If material is not included in the article's Creative Commons licence and your intended use is not permitted by statutory regulation or exceeds the permitted use, you will need to obtain permission directly from the copyright holder. To view a copy of this licence, visit <http://creativecommons.org/licenses/by-nc-nd/4.0/>.

© The Author(s) 2025